Accepted Manuscript

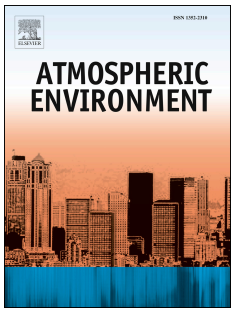

Development of high-resolution dynamic dust source function - A case study with a strong dust storm in a regional model

Dongchul Kim, Mian Chin, Eric M. Kemp, Zhining Tao, Christa D. Peters-Lidard, Paul Ginoux

PII: S1352-2310(17)30215-7

DOI: 10.1016/j.atmosenv.2017.03.045

Reference: AEA 15256

To appear in: *Atmospheric Environment*

Received Date: 1 December 2016

Revised Date: 7 March 2017

Accepted Date: 24 March 2017

Please cite this article as: Kim, D., Chin, M., Kemp, E.M., Tao, Z., Peters-Lidard, C.D., Ginoux, P., Development of high-resolution dynamic dust source function - A case study with a strong dust storm in a regional model, *Atmospheric Environment* (2017), doi: 10.1016/j.atmosenv.2017.03.045.

Development of High-Resolution Dynamic Dust Source Function - A Case Study with a Strong Dust Storm in a Regional Model

Dongchul Kim[a,*], Mian Chin[b], Eric M. Kemp[c], Zhining Tao[a], Christa D. Peters-Lidard[d], Paul Ginoux[e]

[a] USRA at GSFC, Code 614, NASA Goddard Space Flight Center, Greenbelt, MD, USA

[b] Code 614, NASA Goddard Space Flight Center, Greenbelt, MD, USA

[c] SSAI at GSFC, Code 606.0, NASA Goddard Space Flight Center, Greenbelt, MD, USA

[d] Code 610, NASA Goddard Space Flight Center, Greenbelt, MD, USA

[e] NOAA, Geophysical Fluid Dynamics Laboratory, Princeton, NJ, USA

[*] Corresponding author. Tel.: +1 301 614 6972; fax: +1 301 614 5903.

E-mail address: dongchul.kim@nasa.gov (D. Kim).

Abstract

A high-resolution dynamic dust source has been developed in the NASA Unified-Weather Research and Forecasting (NU-WRF) model to improve the existing coarse static dust source. In the new dust source map, topographic depression is in 1-km resolution and surface bareness is derived using the Normalized Difference Vegetation Index (NDVI) data from Moderate Resolution Imaging Spectroradiometer (MODIS). The new dust source better resolves the complex topographic distribution over the Western United States where its magnitude is higher than the existing, coarser resolution static source. A case study is conducted with an extreme dust storm that occurred in Phoenix,

Arizona in 02-03 UTC July 6, 2011. The NU-WRF model with the new high-resolution dynamic dust source is able to successfully capture the dust storm, which was not achieved with the old source identification. However the case study also reveals several challenges in reproducing the time evolution of the short-lived, extreme dust storm events.

Keywords:
NU-WRF, GOCART, Dust, Dynamic dust source, Arizona dust storm

1. Introduction

Dust is one of the most abundant aerosol types in the atmosphere, playing an important role in the Earth's radiation budget, cloud formation, atmospheric dynamics, and ocean biogeochemistry in various spatial and temporal scales (Husar et al., 2001; Haywood et al., 2005; Jickells et al., 2005; Forster et al., 2007; Evan et al., 2008). Mineral dust is also a major air pollutant that causes premature deaths by cardiopulmonary disease and lung cancer for the countries around the source region (Giannadaki et al., 2014; Sprigg et al., 2014; Morman and Plumlee, 2014). The impact of dust is not limited to source areas but extends to larger regional or even global scales (Carlson and Prospero, 1972; Prospero and Lamb, 2003; Kaufman et al., 2005; Chin et al., 2007; Shao et al., 2010; Yu et al., 2012).

The majority of global dust loading is concentrated near the sources in the permanent desert regions (so-called desert-belt), including North Africa, Middle East, and East Asia (Prospero et al., 2002; Chin et al., 2009; Huneeus et al., 2011; Ginoux et

al., 2012). However, dust is also emitted from semi-arid regions such as the Sahel and inner Mongolia, as well as from agricultural areas. Although dust aerosol generated from semi-arid and agricultural areas is much less than that from the major deserts, its importance for air quality and human health is greater at local- and regional-scales due to their proximity to populated areas. Correctly identifying the dust source locations and representing the dust storm events in numerical models are keys to estimate the impacts of dust on the environment and society.

We present here the dust simulation with the NASA Unified-Weather Research and Forecast (NU-WRF) modeling system (Peters-Lidard et al., 2015). The objective of this paper is two-fold. The first goal is to describe a new, high spatial resolution (1-km) dynamic dust source ($S_{dynamic}$) for NU-WRF that represents an improvement of the existing static dust source (S_{static}) at 0.25°×0.25° resolution (described below) currently available in the community WRF-Chem model. The second goal is to evaluate the NU-WRF model simulation of an extreme dust storm case which occurred in Phoenix, Arizona at 02-03 UTC July 6 (or 19-20 MST, July 5), 2011. While systematic observation for a severe dust storm is rare, we revisit the Phoenix dust storm which has been relatively better documented by observations from various platforms, including visual, surface radar, and surface stations (e.g., Raman et al., 2014; Vukovic et al., 2014). They also provide the meteorological background about the extreme dust storm. Through qualitative and quantitative comparisons with these direct and indirect observations, we discuss details about the simulated dust storm, meteorological conditions, dust source, and surface- and columnar intensity of the dust storm.

In section 2, the high-resolution dynamic dust source in the NU-WRF/GOCART dust emission parameterization and the model experiment setup are described. The case study of the Phoenix dust storm is presented in section 3. In section 4, we discuss the challenges in dust simulation, followed by the summary in section 5.

2. Method

2.1. Dust emission parameterization and source function

The dust emission module in NU-WRF is based on the mechanisms from the Goddard Chemistry Aerosol Radiation and Transport (GOCART) model (Ginoux et al., 2001). Dust emission in GOCART, assuming that the soil mobilization is proportional to the horizontal wind speed at near surface, is parameterized with the 10-m wind speed, the threshold velocity of wind erosion, and the surface condition for each dust size group from 0.1 to 10 μm in radius (Ginoux et al., 2001, 2004; Chin et al., 2009). For each size group with effective radius r, dust emission flux F (μg m^{-2} s^{-1}) is expressed as:

$$F(r) = C\,S\,s(r)\,u^2_{10\mathrm{m}}(u_{10\mathrm{m}} - u_t(r,w)),\ \text{if}\ u_{10\mathrm{m}} > u_t \quad (1)$$

where C is a dimensional factor (0.4 μg s^2 m^{-5} for the current study), S is the dust source function or probability of dust uplifting with a value between 0 and 1, $s(r)$ is the fraction of size group r within the soil, $u_{10\mathrm{m}}$ is the 10m wind speed (m s^{-1}), and u_t is the threshold velocity of wind erosion as a function of dust density, particle diameter, and surface wetness to account for the bonding effect between water and particles (Ginoux et al., 2001, 2004). There are five mass size classes in the GOCART scheme with the respective size ranges of 0.1-1μm, 1-1.8μm, 1.8-3μm, 3-6μm, and 6-10μm. The first group is clay

93 that accounts for 0.1 of the total dust mass. The balanced mass is evenly distributed to the
94 remaining 4 dust size groups that are all silt. In the optical property calculations, the clay
95 group is further split into four groups (0.1-0.18, 0.18-0.3, 0.3-0.6, 0.6-1) with mass
96 fractions of 0.9, 8.1, 23.4, and 67.6%, respectively (Tegen and Fung, 1994).
97 The topographic depression (*H*) and surface bareness (*B*) are two key parameters
98 used in the GOCART scheme to calculate the dust source function (*S*), while other
99 parameters such as soil temperature, surface wetness, and snow cover are also included in
100 *S* calculation. The dimensionless topographic depression term *H* is defined as equation 2.
101 *H* represents the probability of accumulated sediments, based on the consideration that
102 dust sediments from surface erosion are accumulated in valleys and surface depressions
103 (Ginoux et al., 2001; Prospero et al., 2002):
104
105 $$H = \left(\frac{z_{max} - z}{z_{max} - z_{min}}\right)^5 \quad (2)$$
106
107 where *z* is the altitude of a grid cell, and z_{max} and z_{min} are the maximum and minimum
108 elevations of topography in the surrounding 10°×10° search area. The fifth order power is
109 applied to increase the topographic contrast.
110 In the community WRF-Chem/GOCART, *H* (0.25°×0.25°) is generated with the
111 GOCART scheme based on the topography and land mask from the Geophysical Fluid
112 Dynamics Laboratory C360 High Resolution Atmospheric Model (~0.24° resolution)
113 which are derived from the 5 min NAVY data (Ginoux et al., 2001; Putman and Lin,
114 2007). The bare soil surface in the community WRF-Chem/GOCART was determined
115 based on the 8 km land-cover data from the Advanced Very High Resolution Radiometer

(AVHRR) satellite (DeFries et al., 1998) and it does not resolve the temporal variations of vegetation cover.

Recently, Kim et al. (2013) have described a method of constructing a global dynamic surface bareness (*B*) in 1°×1° spatial resolution using the 8-km spatial resolution AVHRR Normalized Difference Vegetation Index data (NDVI). Calculated from the visible (VIS) and near-infrared (NIR) radiation, NDVI reflects the state of vegetation over surface (Tucker, 1979):

$$NDVI = (NIR-VIS)/(NIR+VIS) \quad (3)$$

MODIS NDVI has been applied for recent dust simulation studies either as a source masking (Vukovic et al., 2014) or as a surface vegetation fraction which is an input parameter for surface roughness estimation (Xi and Sokolik, 2015). In the present study MODIS NDVI is used to derive surface bareness following Kim et al. (2013). The surface is considered erodible when NDVI is below the threshold NDVI value (i.e., $NDVI_{thr}$). The $NDVI_{thr}$ has been set to 0.15 taking the fact that the typical NDVI values are 0.05~0.10 over bare ground and the values gets larger than 0.2 during growing season over semi-arid region such as grass or shrub land (Huete, 1999; Zeng et al., 2000; Miller et al., 2006; Kim et al. 2013), such that the surface bareness *B* is determined as

$$B = \begin{cases} 1, & NDVI < NDVI_{thr} \\ 0, & otherwise \end{cases} \quad (4)$$

Keeping the principles of the original dynamic dust emission parameterization, the present study has made two major improvements. First, the degree of topographic depression (*H*) has been calculated using the U.S. Geological Survey (USGS) global topography map in 30 arc-second (~1-km) resolution (GTOPO30; USGS, 1996) within a larger search area (12°×12°). Second, the surface bareness (*B*) is constructed using daily MODIS NDVI data in 0.01° (~1-km) resolution over North America (Case et al., 2014). The high resolution topographic and source function better resolves the complex geographical variability especially over the western United States (Figure 1a and 1b). The MODIS NDVI for July 2011 shows a strong spatial variation ranging from 0.1 to 0.8 (Figure 1c). The erodible bare-ground (i.e., NDVI <0.15) appears over the western United States (Figure 1d).

2.2. Model description and experimental setup

The high-resolution dynamic dust source function has been implemented to the NU-WRF modeling system developed at NASA with collaborations with other agencies and institutions. NU-WRF is an observation-driven integrated modeling system that represents aerosol, cloud, precipitation and land processes at satellite-resolved scales at 1 to a few km (Peters-Lidard et al., 2015). NU-WRF is built upon the Advanced Research WRF (ARW; Skamarock et al. 2008) dynamical core model and the WRF-Chem (Grell et al., 2005), with additional NASA components that include the Goddard Land Information System (LIS; Kumar et al. 2006; Peters-Lidard et al. 2007), the GOCART aerosol modules in WRF-Chem (Tao et al., 2013), the Goddard radiation and cloud microphysics schemes (Tao et al. 2003; Lang et al. 2007, 2011; Shi et al. 2014), and the Goddard

Satellite Data Simulator Unit (G-SDSU; Matsui et al., 2013, 2014).

For the case study, we have chosen a dust storm event that occurred in Phoenix, Arizona on 02-03 UTC July 6, 2011. The U.S. National Weather Service has reported that the Phoenix dust storm of July 5, 2011 is one of the most extreme storms in the last 30 years (http://www.wrh.noaa.gov/psr/pns/2011/July/DustStorm.php), with an estimated dust front size of 160 km, depth of 18 km, and top height of 1500-1800 m. Physical characteristics of the dust storm and its meteorological system were analyzed by previous studies (Raman et al., 2014; Sprigg et al., 2014; Vukovic et al., 2014).

In our study, a single domain encompasses 500×500 km^2 with the 1-km horizontal resolution centered at the Phoenix KIWA Weather Surveillance Radar – 1988 Doppler (WSR-88D) station (111.6W, 33.3N). A terrain-following, pressure-based vertical coordinate is used (Skamarock et al, 2008) and consists of 31 layers with a model top pressure of 50 hPa. The model integration time step is set to 3 seconds. The model was simulated for 48 hours, from 00 UTC 5 July, 2011 to 00 UTC 7 July, 2011. Table 1 summarizes the NU-WRF configuration options selected for various atmospheric processes. Initial and lateral boundary conditions for meteorological variables were obtained from the NCEP Global Forecasting System (GFS). The NU-WRF/GOCART simulations were also conducted for anthropogenic aerosols using GOCART aerosol model and its contribution to PM10 is less than a few $\mu g\ m^{-3}$ during the storm. For the case study, the empirical dimensional factor (C) is set to 0.4, emitted dust is equally distributed to the lowest 5 model layers which extend to about 500 m above ground level (AGL), and the cutoff soil moisture factor (g_{wet}) is set to 0.35. In the present case study,

183 we only consider dust aerosol because of the negligible level of other aerosols during the
184 dust storm.
185
186 3. Results of the case study
187 3.1. Phoenix dust storm on July 5, 2011
188 The U.S. National Weather Service has reported that strong thunderstorms
189 developed east of Tucson, AZ during the afternoon local hours of July 5, 2011
190 (http://www.wrh.noaa.gov/psr/pns/2011/July/DustStorm.php). The storms intensified as
191 they progressed west into the Tucson Metropolitan Area, producing downburst winds in
192 excess of 30 m s^{-1}. The leading edge of these strong outflow winds moved to the
193 northwest at 45 to 65 km hr^{-1}. The first dust wall in Casa Grande (which is located at
194 about 75 km southwest of Phoenix) was reported to NWS Phoenix by 06:30 PM MST
195 July 5 (01:30 UTC July 6). The unstable atmosphere with a convective available potential
196 energy of 786 J kg^{-1} marked at the Tucson weather station at 12 UTC July 5, 2011
197 suggests conditions are favorable for a strong thunderstorm.
198 The thunderstorm near Tucson that initiated the Phoenix dust storm is associated
199 with the North American Monsoon (NAM), when the synoptic scale wind and rainfall
200 shifts in the summer over Mexico and the southwestern U.S. (Douglas et al., 1993;
201 Adams and Comrie, 1997). Briefly speaking, the NAM circulation pattern typically
202 develops in late May or early June over southwest Mexico, moving to northwest Mexico
203 in mid to late June, and to the southern U.S. in early July
204 (http://www.wrh.noaa.gov/twc/monsoon/monsoon_NA.php). In the NAM, the low level
205 moisture is transported primarily from the Gulf of California and eastern Pacific. The

upper level moisture is transported mainly from the Gulf of Mexico by easterly winds. Since the lower level moisture flow is not as persistent, the state of the upper level atmosphere is important for thunderstorm development on a given day. In addition, the southwestern U.S. was experiencing a moderate to extreme drought in 2011 according to the U.S. National Drought Monitor (http://www.drought.gov/drought/). The barren surface resulting from the drought provides more favorable conditions for dust emission.

The Phoenix KIWA radar (111.6°W, 33.3°N, 412 m Mean Sea Level, MSL) was operating during the Phoenix dust storm event. Although the main application of Next Generation Weather Radar Level-III (NEXRAD Level-III) is for weather analysis and forecasts, previous studies (e.g., Raman et al., 2014; Vukovic et al., 2014) have used it to probe the location, area, and motion of dust storm since more reliable and continuous dust storm observations are absent. The radar data is available with 5-minute frequency at the National Centers for Environmental Information NEXRAD online data inventory (http://www.ncdc.noaa.gov/nexradinv/index.jsp). In Figure 2, we show hourly radar reflectivity, co-polar correlation coefficient, and base velocity from the NEXRAD Level-III at 0.5° elevation angle between 01:30 to 03:32 UTC. The radar reflectivity is the returned signal within a sampling volume to the radar station. The co-polar correlation coefficient is the correlation between the backscattered horizontal and vertical polarized signals ranging zero (i.e., non-spherical shape) and one (i.e., spherical shape). The base velocity is the measure of the radial component of the wind either negative (i.e., toward) or positive (i.e., away) values from the radar. Although limited, the strong dust storm can be identified with combined analysis of the radar and surface observations.

At 01:30 UTC July 6, the radar showed well-defined bow shape in the

229 southeastern area of the KIWA as marked with an arrow in Figure 2a. The bow shape is
230 characterized with weak reflectivity (<20 dBZ), low co-polar correlation coefficient
231 (<0.8), and a stronger wind (20 knots or 10 m s^{-1}) toward KIWA. Combined with the
232 visual observations by NWS reports, previous studies (e.g., Raman et al., 2014; Vukovic
233 et al., 2014) have suggested that the bow shape is the dust storm that hit the Phoenix
234 Metropolitan area. At 02:31 UTC, the dust front moves toward the KIWA radar station
235 with the extended front size. The wind front passed the radar station and the sign of the
236 base radial velocity is now positive. At 03:32 UTC, the dust storm continues moving
237 toward the northwest and the front is located inside of the Phoenix Metropolitan area
238 (i.e., the area of the white rectangle). Key information from the radar analysis includes:
239 (1) the maximum of the base velocity is larger than 23 ms^{-1} (or 45 knots) and its origin is
240 located at the southeast of Phoenix near Tucson; (2) the front moves toward northwest
241 with a speed in 50-60 km $hour^{-1}$; and (3) the major dust storm area covers Phoenix at 02-
242 03 UTC and its front expands more than 150 km.
243
244 3.2. NU-WRF simulation of the Phoenix dust storm
245 From this section, our case study domain covers 500 km × 500 km centered on the
246 KIWA radar station. The 1-km topography map shows that the northeastern region of the
247 domain mainly consists of mountains higher than 1500 m, while the southwestern region
248 consists of lower terrain with heights below 500 m (Figure 3a). *H* is low over the
249 mountain regions (<0.1) but it is higher over the coastal regions and basins (>0.2) due to
250 the inverse relationship with topography (Figure 3b). The surface conditions are
251 characterized by the arid southwestern region with the NDVI below 0.15, and the

252 vegetated northeastern mountainous region with the NDVI larger than 0.2 (Figure 3c and
253 3d). The resulting high-resolution dynamic dust source function ($S_{dynamic}$) covers most of
254 the southwestern basin region ranging from 0.05 to 0.3, but it excludes most of the
255 northeastern mountains (Figure 3e). In contrast, the static dust source (S_{static}) does not
256 show the detailed geographical structure and its values (mostly below 0.05) are much
257 smaller than those in $S_{dynamic}$ for the same geographic areas (Figure 3f).

258 The horizontal 10-m wind field (W10m) from NU-WRF is plotted every 2 hours
259 during the dust storm (Figure 4). A strong wind area begins to form at 21 UTC July 5,
260 2011 and it develops a clear wind gust front two hours later (23 UTC) over the southern
261 region of the domain. The magnitude of the wind gust continues to intensify and the
262 maximum wind speed rapidly moves toward northwest (01 UTC July 6). The area with
263 strong wind passes through the Phoenix Metropolitan area at 03 UTC. Then it continues
264 to move towards the northwest until it weakens in the next four hours. The maximum
265 simulated wind speed in the study domain during the event is larger than 20 m s^{-1}. The
266 model captures the initial location and fast motion of the storm observed by the radar
267 shown in the previous section. On the other hand, the simulation also shows that the
268 maximum strength of the storm is located further west than the radar observation (i.e.,
269 Figure 2).

270 The temperature contours and y-z component of the cross section wind vector that
271 passes through Phoenix (i.e., shown in Figure 3a) are plotted during the dust storm period
272 from 21 UTC July 5 with a 2-hour interval (Figure 5). At 21 UTC July 5, the vertical
273 atmospheric structure is characterized with the gradual decreasing change of temperature
274 from near surface (> 30°C) to upper air (15°C at 3 km MSL). The north-south wind

vector component is not strong at the time, but the presence of updraft near 31°N indicates that the thunderstorm is beginning to develop. At 23 UTC, the temperature of the lower atmosphere in the south of 32°N significantly drops from 33°C to 24°C as a result of the rain-cooled downburst from the upper atmosphere. At 01 UTC July 6, the strong horizontal blowouts of cold air continue to progress to north. At 03 UTC the strong wind extends to 34°N with the curl shaped wind pattern in the lower atmosphere of 1-3 km MSL. The intensive downburst is dissipated at 05 UTC (Figure 5). Our result is consistent with the NWS report that the explosive horizontal outflow during the Phoenix dust storm was initiated by downburst generated by the thunderstorm, which occurred near the Tucson Metropolitan Area.

Hourly surface meteorology data over the study domain is available from NOAA's National Centers for Environmental Information (NCEI) (https://www7.ncdc.noaa.gov/CDO/cdo). We analyze the time series of meteorological fields of wind speed, temperature, relative humidity, and surface pressure at three airport stations of Tucson (110.96W, 32.13N, 777m), Casa Grande (111.77W, 32.95N, 446m), and Phoenix (112.00W, 33.43N, 337m) and compare them with the NU-WRF model (Figure 6). Located from South to North along the storm track, the station data provides useful insight of the surface meteorological conditions during the storm passage. The most noticeable result form the observation is the rapid change of meteorological fields with the arrival of the storm. At Tucson, for example, the observation shows that the rapid change occurs between 23 UTC July 5 and 01 UTC July 6. Temperature decreases from 36.7 °C to 21.7 °C and wind speed increases from 5.8 ms^{-1} to 8.9 ms^{-1} with the arrival of the storm. The increase of relative humidity from 21% to 82% is explained with

298 the large decrease of temperature. Surface pressure does not vary much ranging from 920
299 to 930 mb. Similar sudden changes appear in the Northern stations of Casa Grande (01-
300 03 UTC July 6) and Phoenix (03-05 UTC July 6), but 2 to 4 hour later than Tucson. At
301 Casa Grande, the temperature and wind speed are changed from 38.9 °C to 23.9 °C and
302 from 1.3 ms^{-1} to 15.2 ms^{-1}, respectively. At Phoenix, the temperature and wind speed are
303 changed from 37.8 °C to 27.2 °C and from 3.6 ms^{-1} to 8.9 ms^{-1}, respectively. NU-WRF
304 model captures the magnitude and pattern of the observation, showing that it can
305 reproduce the storm and its evolution. However the comparison also shows that the
306 simulated storm is moving faster than observation resulting 1 or 2 hour earlier storm
307 arrival at Casa Grande and Phoenix. Daily accumulated precipitation was 25.6 mm at
308 Tucson station, but no precipitation is reported at Phoenix station or negligible at Casa
309 Grande station (<1 mm).

310 The dust emission is plotted in Figure 7, and is mainly controlled by W10m since
311 the dust emission in the NU-WRF/GOCART is proportional to the 3rd order of W10m
312 (Eq. 1). The amount of dust emission exceeds 100 μg m^{-2} s^{-1} during peak dust storm hours
313 of 01-03 UTC. In contrast to the original soil moisture threshold value of $g_{wet} < 0.5$, a
314 reduced threshold values (i.e., $g_{wet} < 0.35$) was used in the current simulation to achieve a
315 better agreement with the radar observation. As a result dust emission over the
316 southwestern region of the domain (i.e., southwest of 113°W, 33°N) is substantially
317 suppressed during the dust storm period. The time-evolution of the surface dust PM10
318 (dust size is less than 10 μm) concentrations is quite similar to that of dust emission
319 (Figure 8). The model simulated PM10 over the Phoenix area (i.e., inside the black
320 square) is less than 100 μg m^{-3} most of time at 01 UTC July 6, 2011. When dust storm

reaches the Phoenix at 03 UTC, the PM10 drastically increases to reach 4000 μg m^{-3}. After the dust storm at 05-07 UTC, the PM10 concentration gradually reduces but still remains much higher than that before the dust storm. In section 4, we will discuss the apparent tardy decay of dust concentrations simulated by the model.

The cross sections of dust concentration and the y-z component of wind vector at 112°W during the dust storm are plotted in Figure 9. At 21-23 UTC July 5, model-simulated dust concentrations are relatively low because of the low emission rates (Figure 7). At 01 UTC July 6, high dust concentration (700-1000 μg m^{-3}) first appears in the latitudinal zone between 32.3°N and 32.8°N that agrees with the horizontal dust surface concentration field in Figure 8. The model shows that at 2 km above the ground the dust concentration is about 100 μg m^{-3}. The high dust concentration area rapidly moves north following the strong horizontal wind gust. At 03 UTC, the front of dust moves about 60 km $hour^{-1}$ reaching to 33.9°N. At the same time, the lofted dust layer (>1 km above surface level) is found behind the dust storm between 32.6°N and 33.9°N. At 05 UTC, dust storm front continues moving north but its moving speed has reduced by about half. However, the surface dust concentration remains high (>1500 μg m^{-3}) at 33-34.5°N after the storm at 05-07 UTC, as shown in Figure 8.

3.3. Comparisons of model simulation with observations

The simulated dust at surface level is compared with the air quality data from the U.S. Environmental Protection Agency's Air Quality System obtained from the EPA's AirData website (http://www.epa.gov/airdata/) (Figure 10). Across the state of Arizona, all of the 13 sites with clear dust storm signals are in and around the Phoenix

Metropolitan area in the range between 113.3°W, 32.0°N and 110.4°W, 34.3°N (i.e., the black box in Figure 3a). All EPA PM10 observations indicate a sharp dust peak that occurred in the two-hour window between 02 to 04 UTC on July 6 with a maximum at 03 UTC, although the PM10 magnitudes vary by location from 1946 to 6348 μg m^{-3}. The model captures the observed peak events at most sites with an averaged value over 13 sites (2968 μg m^{-3}) similar to the observations (2505 μg m^{-3}) and the average correlation coefficient of 0.63. In contrast, a run with the static dust source has simulated only a negligible amount of surface PM10 concentration (81~258 μg m^{-3}) in those EPA stations during the same period (i.e., Figure 10). After the dust storm, the observations show a rapid decrease of dust concentrations at all sites to the pre-storm levels, but the dust concentration in the NU-WRF model remains elevated. This after-peak high bias in the model could be caused by various physical reasons such as the location and progress of dust storm and uncertainties in dry deposition or emission processes. Further investigation with various model runs has found that dust emission from south of the Phoenix area for 2 hours from 0300 UTC July 6 is most responsible to the high bias in the NU-WRF model. A sensitivity simulation that turned off dust emissions after 0300 UTC indeed removes the high dust residual after the storm and improves the correlation coefficient (r=0.89) and other statistics (Figure 11).

4. Discussion

Although the case study shows the high-resolution dynamic dust source considerably improves dust modeling, it also illustrates several outstanding challenges in dust emission processes in the NU-WRF/GOCART model:

(i) The curly motion of the outflowing dust front in the downburst produces the wall of dust, which reached higher than 1.5 km in the 2-3 hour time span. However, the advection/convection scheme in NU-WRF could not resolve the rapid vertical transport of the high dust wall, leaving most of the dust in the lowest levels. In the present case study, we equally distributed the emitted dust to the lowest 5 model layers (which are about 0-500 m above the ground) to better resolve the vertical distribution of the simulated dust. It is necessary to consider a better mechanism to represent the vertical distribution of emitted dust in the "haboob" events.

(ii) Dust emission is inhibited when g_{wet} is larger than the threshold. While g_{wet} values are regionally dependent from 0.35 to 0.5 in global GOCART modeling studies (e.g., Kim et al., 2013; Chin et al., 2014), the threshold g_{wet} of 0.35 is better compared to the observations in the present case study. More robust constrain on the threshold g_{wet} is necessary in future studies.

(iii) The dimensional factor (C) in the global-scale GOCART is set to 1 μg s^2 m^{-5} (Ginoux et al., 2001; Kim et al., 2013). But C values are highly case-dependent, and are in the range from 0.65 to 22 μg s^2 m^{-5} in previous WRF-Chem studies with the static dust source (Zhao et al., 2010; Bian et al., 2011; Alizadeh Choobari et al., 2013; Kumar et al., 2014). In the present extreme dust storm case study, the C value was set to 0.4 μg s^2 m^{-5} to achieve better agreement with the observations. A more generalized method of setting C values is required in future studies.

389 The case study also showed that simulating the correct wind field for calculating
390 dust emission is very important but challenging. Although the NU-WRF used a realistic
391 meteorology (i.e., meteorological fields from reanalysis or model) to initialize simulation
392 and force the lateral boundaries, the location and time evolution of the wind storm within
393 the regional domain are still problematic. For example, the center of the outflowing wind
394 storm in our simulation is positioned too far west compared to the radar. We conducted
395 20 sensitivity runs with different modeling setup and configuration options by varying
396 domain related configurations (initial time, domain nesting, horizontal- and vertical-
397 resolutions) and physics related schemes (planetary boundary layer schemes, longwave-
398 and shortwave-radiation schemes, land-cover, land surface model, initial meteorology
399 input, aerosol radiative feedback, and data assimilation). While most runs successfully
400 captured general characteristics of the Arizona dust storm, no simulation successfully
401 captured the exact timing, location, and evolution of the storm.
402 Similarly to our study, a previous study simulated the Arizona dust storm using
403 the Nonhydrostatic Mesoscale Model on E grid-Dust REgional Atmospheric Model
404 (NMME–DREAM) with 4 km horizontal resolution (Vukovic et al., 2014). The model
405 successfully simulated the position of the front in space and time and horizontal and
406 vertical distribution of dust. Using MODIS NDVI, they have highlighted the importance
407 of vegetation masking to improve dust simulations. Similarly to our modeling study, they
408 also showed some challenging issues in the model results, such as the 1 hour late storm
409 arrival time in Phoenix, underestimations of surface PM10 (<2500 $\mu g\ m^{-3}$), and a strong
410 residual dust 4 hours after the storm (in their Figure 9).
411

5. Summary

In the present study, we have developed a high-resolution dynamic dust source in the NU-WRF model. The source function is calculated from the 1-km topography map and from the surface bareness derived from the dynamic surface vegetation information from MODIS at 1-km resolution. A case study simulating an extreme dust storm occurred in Phoenix, Arizona in 02-03 UTC July 6, 2011 has demonstrated that the new high-resolution dynamic dust source better captures the complex topographic distribution pattern and it simulates the dust storm better than the previously used lower resolution, static dust source in this case. Although there is some discrepancy, the model captures the initial location and fast motion of the storm observed by the radar.

NU-WRF surface dust PM10 is compared with the 13 station data in the EPA's Air Quality System network. The time series analysis shows that NU-WRF can successfully simulate the progress of the Phoenix dust storm (R=0.63) and its magnitude. At the peak hour at Phoenix (03 UTC July 6), the PM10 drastically increased with the observed and simulated station means of 2968 and 2505 $\mu g\ m^{-3}$, respectively. Significantly elevated dust PM10 values after the dust storm (e.g., at 07 UTC) simulated by NU-WRF were found to be due to excess dust emission near the Phoenix region between 03-04 UTC, when the actual dust storm had already passed the city.

The NU-WRF model with the new high-resolution dynamic dust source is able to capture the Phoenix dust storm, which was not possible using the old static sources. However, the case study also has revealed several issues in the NU-WRF/GOCART model to reproduce the rapid change of surface concentrations during the event. The NU-WRF model could not exactly place the location of outflowing winds against radar, even

435 after 20 additional sensitivity runs with different configurations and physics options. This
436 highlights that simulating accurate meteorology and wind fields is highly important for
437 dust storm prediction but it is also a challenging task.
438
439 Acknowledgement
440 This research was funded by the NASA's Modeling, Analysis, and Prediction (MAP)
441 program (Solicitations NNH08ZDA001N-MAP and NNH12ZDA001N-MAP); the
442 NASA's Atmospheric Composition: Modeling and Analysis (ACMAP) program. The
443 authors would like to thank the NASA Center for Climate Simulation (NCCS) for
444 supercomputing and mass storage support. The authors also would like to thank
445 NOAA/NCEI for radar images, the EPA for surface PM10 concentration data, and NASA
446 MODIS and SPoRT teams for NDVI data.

447 References
448
449 Adams, D. K., Comrie, A. C., 1997. The North American Monsoon. Bull. Amer. Meteor.
450 Soc., 78, 2197-2213.

451 Alizadeh-Choobari, O., Zawar-Reza, P., Sturman, A., 2013. Simulation of the spatial
452 distribution of mineral dust and its direct radiative forcing over Australia. *Tellus B, 65*,
453 19856. doi:http://dx.doi.org/10.3402/tellusb.v65i0.19856.

454 Bian, H., Tie, X., Cao, J., Ying, Z., Han, S., Xue, Y., 2011. Analysis of a severe dust
455 storm event over China: application of the WRF-Dust model. Aerosol and Air Quality
456 Res., 11, 419–428.

457 Carlson, T. N., and Prospero, J. M., 1972. The Large-scale movement of Saharan air
458 outbreaks of the Northern Equatorial Atlantic. J. Appl. Meteorol., 11, 283-297.

459 Case, J.L., LaFontaine, F.J., Bell, J.R., Jedlovec, G.J., Kumar, S.V., Peters-Lidard, C.D.,
460 2014. A real-time MODIS vegetation product for land surface and numerical weather
461 prediction models. IEEE Trans. Geosci. Remote Sens., 52 (3), 1772-1786.
462 http://dx.doi.org/10.1109/TGRS.2013.2255059.

463 Chin, M., Diehl, T., Ginoux, P., Malm, W., 2007. Intercontinental transport of pollution
464 and dust aerosols: implications for regional air quality. Atmos. Chem. Phys., 7, 5501-
465 5517.

466 Chin, M., Diehl, T., Dubovik, O., Eck, T.F., Holben, B.N., Sinyuk, A., Streets, D.G.,
467 2009. Light absorption by pollution, dust and biomass burning aerosols: a global model
468 study and evaluation with AERONET data. Ann. Geophys., 27, 3439-3464.

469 Chin, M. Diehl, T., Tan, Q., Prospero, J. M., Kahn, R. A., Remer, L. A., Yu, H., Sayer,
470 A. M., Bian, H., Geogdzhayev, I. V., Holben, B. N., Howell, S. G., Huebert, B. J., Hsu,
471 N. C., Kim, D., Kucsera, T. L., Levy, R. C., Mishchenko, M. I., Pan, X., Quinn, P. K.,
472 Schuster, G. L., Streets, D. G., Strode, S. A., Torres, O., and Zhao, X.-P., 2014. Multi-
473 decadal aerosol variations from 1980 to 2009: a perspective from observations and a
474 global model. Atmos. Chem. Phys., 14, 3657-3690. doi:10.5194/acp-14-3657-2014.

475 DeFries, R., Hansen, M., Townshend, J., Sohlberg, R., 1998. Global land cover
476 classification at 8km spatial resolution: The use of training data derived from Landsat
477 imagery in decision tree classifiers. Int. J. Remote Sens., 19, 3141-3168.

478 Douglas, M.W., Maddox, R.A., Howard, K, Reyes, S., 1993. The Mexican monsoon. J.
479 Climate, 6, 1665-1667.

480 Evan, A. T., Heidinger, A. K., Bennartz, R., Bennington, V., Mahowald, N. M., Corrada-
481 Bravo, H., Velden, C. S., Myhre, G., Kossin, J. P., 2008. Ocean temperature forcing by
482 aerosols across the Atlantic tropical cyclone development region. Geochem. Geophy.
483 Geosy., 9, Q05V04. doi:10.1029/2007GC001774.

484 Forster, P., Ramaswamy, V., Artaxo, P., Berntsen, T., Betts, R., Fahey, D. W., Haywood,
485 J., Lean, J., Lowe, D. C., Myhre, G., Nganga, J., Prinn, R., Raga, G., Schulz, M., and Van
486 Dorland, R., 2007. Changes in Atmospheric Constituents and in Radiative Forcing, in:
487 Climate Change 2007: *The Physical Science Basis, contribution of Working Group I to*

the Fourth Assessment Report of the Intergovernmental Panel on Climate Change, edited by: Solomon, S. D., Qin, M., Manning, Z., Chen, M., Marquis, K. B., Averyt, M. T., and Miller, H. L., Cambridge University Press, Cambridge, United Kingdom and New York, NY, USA, 129–234.

Giannadaki, D., Pozzer, A., and Lelieveld, J., 2014. Modeled global effects of airborne desert dust on air quality and premature mortality. Atmos. Chem. Phys., 14, 957-968, doi:10.5194/acp-14-957-2014.

Ginoux, P., Chin, M., Tegen, I., Prospero, J. M., Holben, B., Dubovik, O., Lin, S.-J., 2001. Sources and distributions of dust aerosols simulated with the GOCART model. J. Geophys. Res., 106 (D17), 20255-20273. http://dx.doi.org/10.1029/2000JD000053.

Ginoux, P., Prospero, J. M., Torres, O., and Chin, M., 2004. Long-term simulation of global dust distribution with the GOCART model: Correlation with the North Atlantic Oscillation. Environ. Model. Software, 19, 113-128. doi:10.1016/S1364-8152(03)00114-2.

Ginoux, P., Garbuzov, D., Hsu, N. C., 2010. Identification of anthropogenic and natural dust sources using Moderate Resolution Imaging Spectroradiometer (MODIS) Deep Blue level 2 data. J. Geophys. Res., *115*, D05204. doi:10.1029/2009JD012398.

Ginoux, P., Prospero, J. M., Gill, T. E., Hsu, N. C., and Zhao, M., 2012. Global-scale attribution of anthropogenic and natural dust sources and their emission rates based on MODIS Deep Blue aerosol products. Rev. Geophys., 50, RG3005, doi:10.1029/2012RG000388.

Grell, G. A., Peckham, S. E., Schmitz, R., and McKeen, S. A., Frost, G., Skamarock, W. C., Eder, B., 2005. Fully coupled "online" chemistry within the WRF model, Atmos. Environ., 39, 6957–6976.

Haywood, J. M., Allan, R. P., Culverwell, I., Slingo, A., Milton, S., Edwards, J., Clerbaux, N., 2005. Can desert dust explain the outgoing longwave radiation anomaly over the Sahara during July 2003?, J. Geophys. Res., 110, D05105. doi:10.1029/2004JD005232.

Huete, A.R., Justice, C. and Leeuwen, van W., 1999. MODIS vegetation index (MOD 13), Algorithm theoretical basis document ATBD13. http://modis.gsfc.nasa.gov/data/atbd/atbd_mod13.pdf. (Accessed on October 28, 2016).

Huneeus, N., Schulz, M., Balkanski, Y., Griesfeller, J., Prospero, J., Kinne, S., Bauer, S., Boucher, O., Chin, M., Dentener, F., Diehl, T., Easter, R., Fillmore, D., Ghan, S., Ginoux, P., Grini, A., Horowitz, L., Koch, D., Krol, M. C., Landing, W., Liu, X., Mahowald, N., Miller, R., Morcrette, J.-J., Myhre, G., Penner, J., Perlwitz, J., Stier, P., Takemura, T., and Zender, C. S., 2011. Global dust model intercomparison in AeroCom phase I. Atmos. Chem. Phys., 11, 7781–7816. doi:10.5194/acp-11-7781-2011.

Husar, R. B., et al., 2001. Asian dust events of April 1998. J. Geophys. Res., 106, 18,317–18,330.

Jickells, T. D., et al., 2005. Global iron connections between desert dust, ocean biogeochemistry, and climate. Science, 308, 67–71.

Kaufman, Y. J., Koren, I., Remer, L. A., Tanré, D., Ginoux, P., Fan, S., 2005. Dust transport and deposition observed from the Terra-Moderate Resolution Imaging Spectroradiometer (MODIS) spacecraft over the Atlantic Ocean. J. Geophys. Res., 110, D10S12. doi:10.1029/2003JD004436.

Kim, D., Chin, M., Bian, H., Tan, Q., Brown, M., Zheng, T., You, R., Diehl, T., Ginoux, P., Kucsera T., 2013. The Effect of the Dynamic Surface Bareness on Dust Source Function, Emission, and Distribution. J. Geophy. Res., 118, 871-886. doi:10.1029/2012JD017907.

Kumar, S.V., Peters-Lidard, C.D., Tian, Y., Houser, P.R., Geiger, J., Olden, S., Lighty, L., Eastman, J.L., Doty, B., Dirmeyer, P., Adams, J., Mitchell, K., Wood, E.F., Sheffield, J., 2006. Land information system: an interoperable framework for high resolution land surface modeling. Environ. Model. Softw., 21 (10), 1402-1415. http://dx.doi.org/10.1016/j.envsoft.2005.07.004.

Kumar, R., Barth, M.C., Pfister, G.G., Naja, M., Brasseur, G.P., 2014. WRF-Chem simulations of a typical pre-monsoon dust storm in northern India: influences on aerosol optical properties and radiation budget. Atmos. Chem. Phys., 14, 2431-2446.

Lang, S., Tao,W.-K., Cifelli, R., Olson, W., Halverson, J., Rutledge, S., Simpson, J., 2007. Improving simulations of convective system from TRMM LBA: easterly and Westerly regimes. J. Atmos. Sci., 64, 1141-1164.

Lang, S., Tao, W.-K., Zeng, X., Li, Y., 2011. Reducing the biases in simulated radar reflectivities from a bulk microphysics scheme: tropical convective systems. J. Atmos. Sci., 68, 2306-2320.

Matsui, T.T., Iguchi, X., Li, M., Han, W.-K., Tao, W., Petersen, T., L'Ecuyer, R., Meneghini, W., Olson, C.D., Kummerow, A.Y., Hou, M.R., Schwaller, E.F., Stocker, J. Kwiatkowski, 2013. GPM satellite simulator over ground validation sites. Bull. Am. Meteor. Soc., 94, 1653-1660. http://dx.doi.org/10.1175/BAMS-D-12-00160.1.

Matsui, T., Santanello, J., Shi, J.J., Tao, W.-K., Wu, D., Peters-Lidard, C., Kemp, E., Chin, M., Starr, D., Sekiguchi, M., Aires, F., 2014. Introducing multi-sensor satellite radiance-based evaluation for regional earth system modeling. J. Geophys. Res. Atmos., 119, 8450-8475. http://dx.doi.org/10.1002/2013JD021424.

Miller, J., Barlage, M., Zeng, X., Wei, H., Mitchell, K., Tarpley, D., 2006. Sensitivity of the NCEP/Noah land surface model to the MODIS green vegetation fraction data set. Geophys. Res. Lett., 33, L13404. doi:10.1029/2006GL026636.

Morman, S.A., Plumlee, G. S., 2014. Dust and Human Health. In Mineral Dust: A key Player in the Earth System (ed. Knippertz, P. and Stuut, J.B.W.). pp.385–409. Springer.

Peters-Lidard, C. D., Houser, P. R., Tian, Y., Kumar, S. V., Geiger, J., Olden, S., Lighty, L., Doty, B., Dirmeyer, P., Adams, J., Mitchell, K., Wood, E. F., Sheffield, J., 2007. Highperformance earth system modeling with NASA/GSFC's land information System. Innov. Syst. Softw. Eng., 3 (3), 157-165. http://dx.doi.org/10.1007/s11334-007-0028-x.

570 Peters-Lidard, C.D., et al., 2015. Integrated modeling of aerosol, cloud, precipitation and
571 land processes at satellite-resolved scales. Environmental Modelling & Software, 67,
572 149–159. doi:http://dx.doi.org/10.1016/j.envsoft.2015.01.007.

573 Prospero, J. M., Ginoux, P., Torres, O., Nicholson, S. E., and Gill, T. E., 2002.
574 Environmental characterization of global sources of atmospheric soil dust identified with
575 the Nimbus 7 Total Ozone Mapping Spectrometer (TOMS) absorbing aerosol product.
576 Rev. Geophys., 40, 1002. doi:10.1029/2000RG000095.

577 Prospero, J. M., Lamb, P. J., 2003. African droughts and dust transport to the Caribbean:
578 Climate change implications. Science, 302(5647), 1024–1027.

579 Putman, W. M., Lin, S.-J., 2007. Finite-volume transport on various cubed-sphere grids.
580 J. Comput. Phys., 227, 55–78. doi:10.1016/j.jcp.2007.07.022.

581 Raman, A., Arellano, A. F., Brost, J. J., 2014. Revisiting haboobs in the southwestern
582 United States: An observational case study of the 5 July 2011 Phoenix dust storm. Atmos.
583 Environ., 89, 179–188. doi:10.1016/j.atmosenv.2014.02.026.

584 Shao, Y., Fink, A. H., and Klose, M., 2010. Numerical simulation of a continental-scale
585 Saharan dust event. J. Geophys. Res., 115, D13205. doi:10.1029/2009JD012678.

586 Shi, J. J., Matsui, T., Tao, W.-K., Peters-Lidard, C., Chin, M., Tan, Q., Kemp, E., 2014.
587 Implementation of an aerosol-cloud microphysics-radiation coupling into the
588 nasa unified WRF: simulation results for the 6-7 august 2006 AMMA special
589 observing period. Q. J. R. Meteorol. Soc., http://dx.doi.org/10.1002/qj.2286.

590 Skamarock, W. C., Klemp, J. B., Dudhia, J., Gill, D. O., Barker, D. M., Duda, M. G.,
591 Huang, X.-Y., Wang, W., Powers, J. G., 2008. A Description of the Advanced Research
592 WRF Version 3. NCAR Technical Note, NCAR/TN-475flSTR, 113 pp.

593 Sprigg, W. A., Nickovic, S., Galgiani, J. N., Pejanovic, G., Petkovic, S., Vujadinovic, M.,
594 Vukovic, A., Dacic, M., DiBiase, S., Prasad, A., El-Askary, H., 2014. Regional dust
595 storm modeling for health services: the case of valley fever. Aeolian Res., 14, 53–73.

596 Tao, W.-K., Simpson, J., Baker, D., Braun, S., Chou, M.-D., Ferrier, B., Johnson, D.,
597 Khain, A., Lang, S., Lynn, B., Shie, C.-L., Starr, D., Sui, C.-H., Wang, Y., Wetzel, P.,
598 2003. Microphysics, radiation and surface processes in the Goddard Cumulus Ensemble
599 (GCE) model, A special issue on non-hydrostatic mesoscale Modeling. Meteorol. Atmos.
600 Phys., 82, 97-137.

601 Tao, W.-K., Wu, D., Matsui, T., Peters-Lidard, C., Lang, S., Hou, A., Rienecker, M.,
602 Petersen, W., Jensen, M., 2013. Precipitation intensity and variation during
603 MC3E: a numerical modeling study. J. Geophys. Res., 118 (13), 7199-7218.
604 http://dx.doi.org/10.1002/jgrd.50410.

605 Tegen, I., Fung, I., 1994. Modeling of mineral dust in the atmosphere: Sources, transport,
606 and optical thickness. J. Geophys. Res., 99, 22897-22914.

607 Tucker, C. J., 1979. Red and photographic infrared linear combinations formonitoring
608 vegetation. Remote Sensing of Environment, 8, 127−150.

609 USGS, 1996, GTOPO30 documentation, Tech. Rep., U. S. Geol. Surv.
610 https://lta.cr.usgs.gov/sites/default/files/GTOPO30_README.doc

611 Vukovic, A., Vujadinovic, M., Pejanovic, G., Andric, J., Kumjian, M. R., Djurdjevic, V.,
612 Dacic, M., Prasad, A. K., El-Askary, H. M., Paris, B. C., Petkovic, S., Nickovic, S., and
613 Sprigg, W. A., 2014. Numerical Simulation of “an American Haboob”. Atmos. Chem.
614 Phys., 14, 3211-3230. doi:10.5194/acp-14-3211-2014.

615 Xi, X. and Sokolik, I. N., 2015. Seasonal dynamics of threshold friction velocity and dust
616 emission in Central Asia. J. Geophys. Res. Atmos., 120, 1536–1564,
617 doi:10.1002/2014JD022471.

618 Yu, H., Remer, L.A., Chin, M., Bian, H., Tan, Q., Yuan, T., et al., 2012. Aerosols
619 fromoverseas rival domestic emissions over North America. Science, 337, 566–569.
620 http://dx.doi.org/10.1126/science.1217576.

621 Zeng, X., Dickinson, R. E., Walker, A., Shaikh, M., DeFries, R. S., Qi, J., 2000.
622 Derivation and evaluation of global 1–km fractional vegetation cover data for land
623 modeling. J. Appl. Meteorol., 39, 826–839.

624 Zhao, C., Liu, X., Leung, L. R., Johnson, B., McFarlane, S. A., Gustafson Jr., W. I., Fast,
625 J. D., and Easter, R., 2010. The spatial distribution of mineral dust and its shortwave
626 radiative forcing over North Africa: modeling sensitivities to dust emissions and aerosol
627 size treatments, Atmos. Chem. Phys., 10, 8821–8838. doi:10.5194/acp-10-8821-2010.
628

Table 1. NU-WRF physics setup

Processes Name	Setup
Longwave radiation	Goddard
Shortwave radiation	Goddard
Surface layer	Monin-Obukhov
Land surface	Noah LSM
Boundary layer	YSU
Cumulus clouds	Explicit

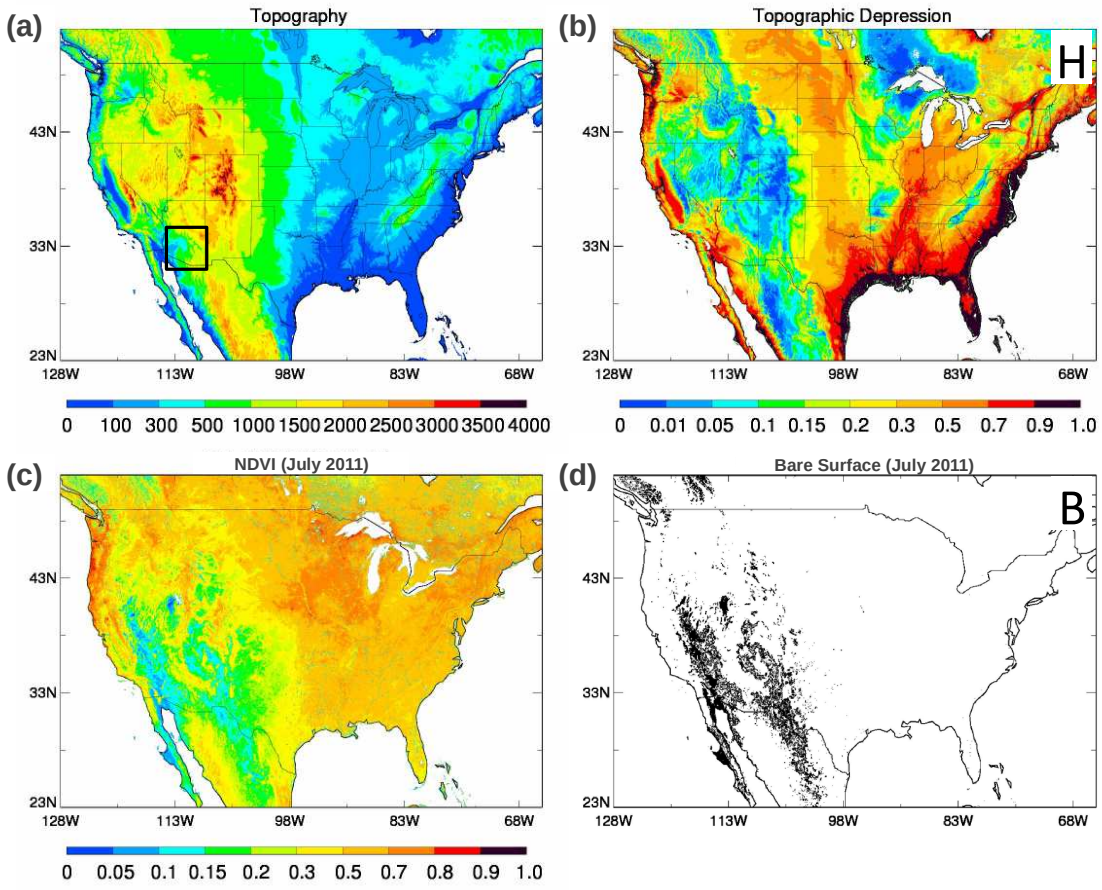

Figure 1. (a) Surface elevation (m), (b) degree of topographic depression (H), (c) MODIS NDVI for July 2011, and (d) location of surface bareness (B) over North America. Black square in (a) is the model domain for the case study.

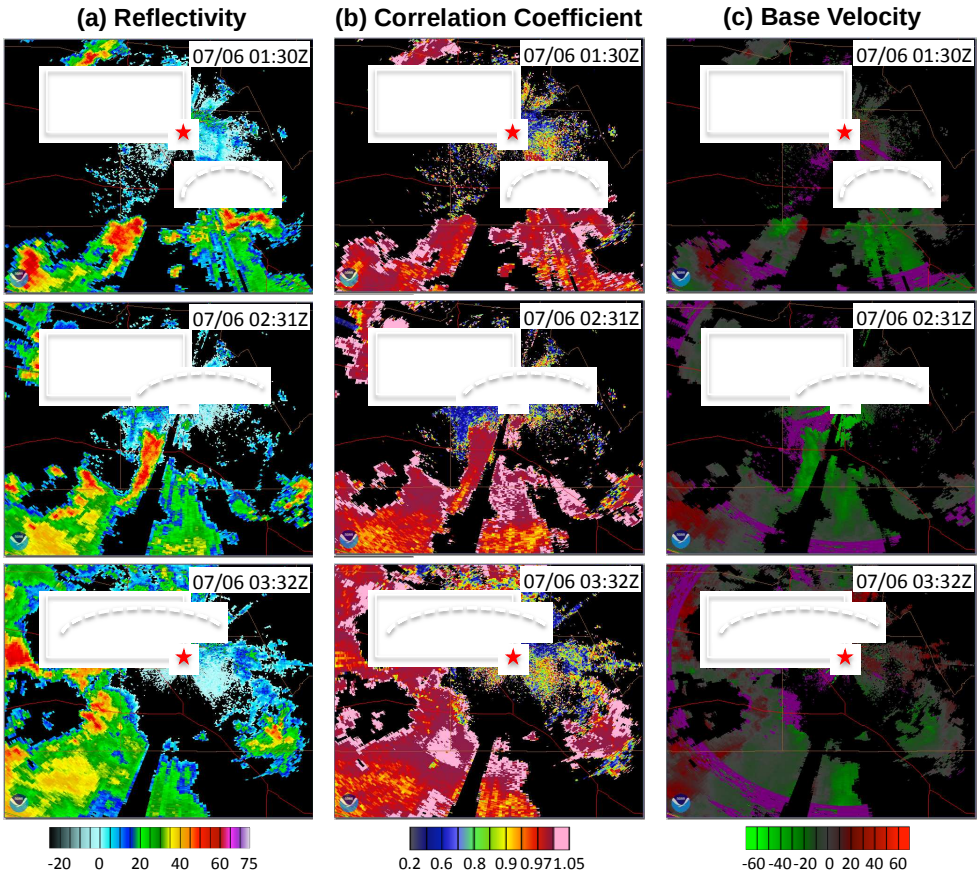

Figure 2. (a) Radar reflectivity in dBZ, (b) co-polar correlation coefficient, and (c) base velocity in knots (1 knot=0.51ms^{-1}) at 0.5° elevation angle from the NEXRAD Level-III during the dust storm event between 0130-0332 UTC July 6, 2011. The location of the KIWA radar station (111.6°W, 33.3°N, 412m) is marked as star symbol. The wind direction is toward the radar when the base velocity is negative or vice versa. Thick dashed-lines indicate the location of dust storm front. Domain covers [113.2°W~110.61°W; 32.0°N~34.1°N] and the white rectangle is the Phoenix metropolitan area which is mixed with some shrublands and grasslands.

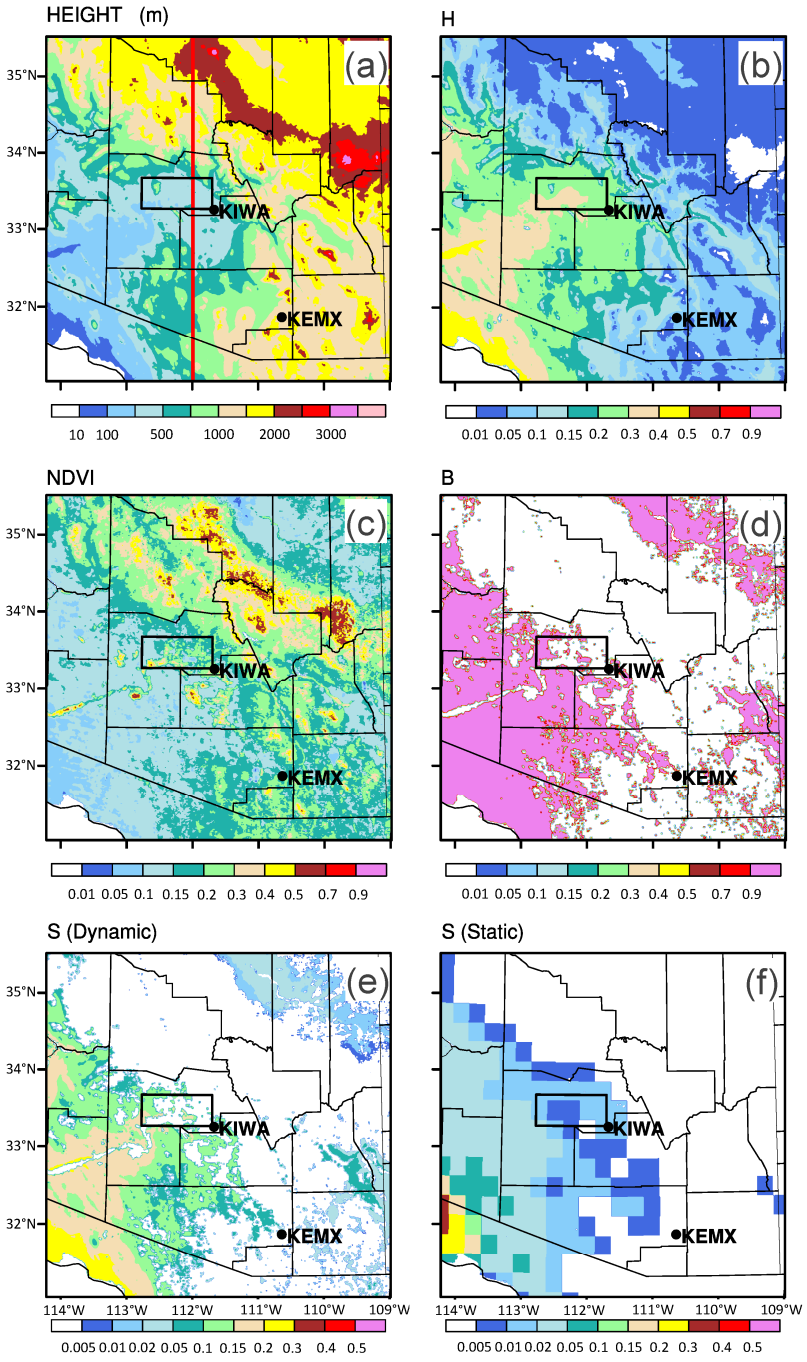

Figure 3. Surface elevation (m), topographic depression (H), NDVI, bareness (B), dynamic source function ($S_{Dynamic}$), and static source function (S_{Static}) over the dust storm case study domain on July 5, 2011. Phoenix Metropolitan is located within the black box. KIWA and KEMX are radar stations at Phoenix and Tucson.

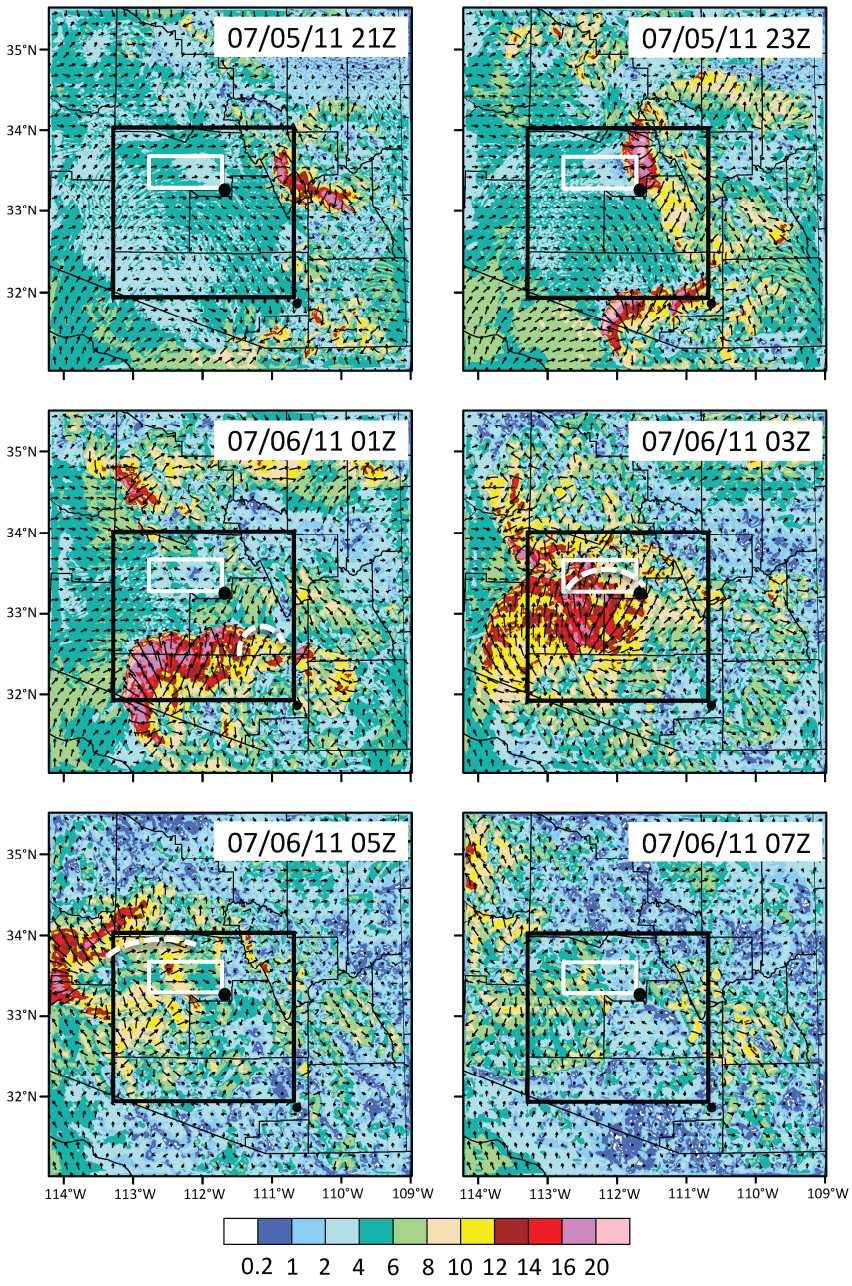

Figure 4. NU-WRF 10-m wind speed (ms^{-1}) and vector over the study domain from 21 UTC July 5 to 07 UTC July 6, 2011. Black square indicates the NEXRAD radar domain shown in Figure 2 and white rectangle is the Phoenix Metropolitan area. Thick dashed-lines indicate the location of dust storm front from radar observation.

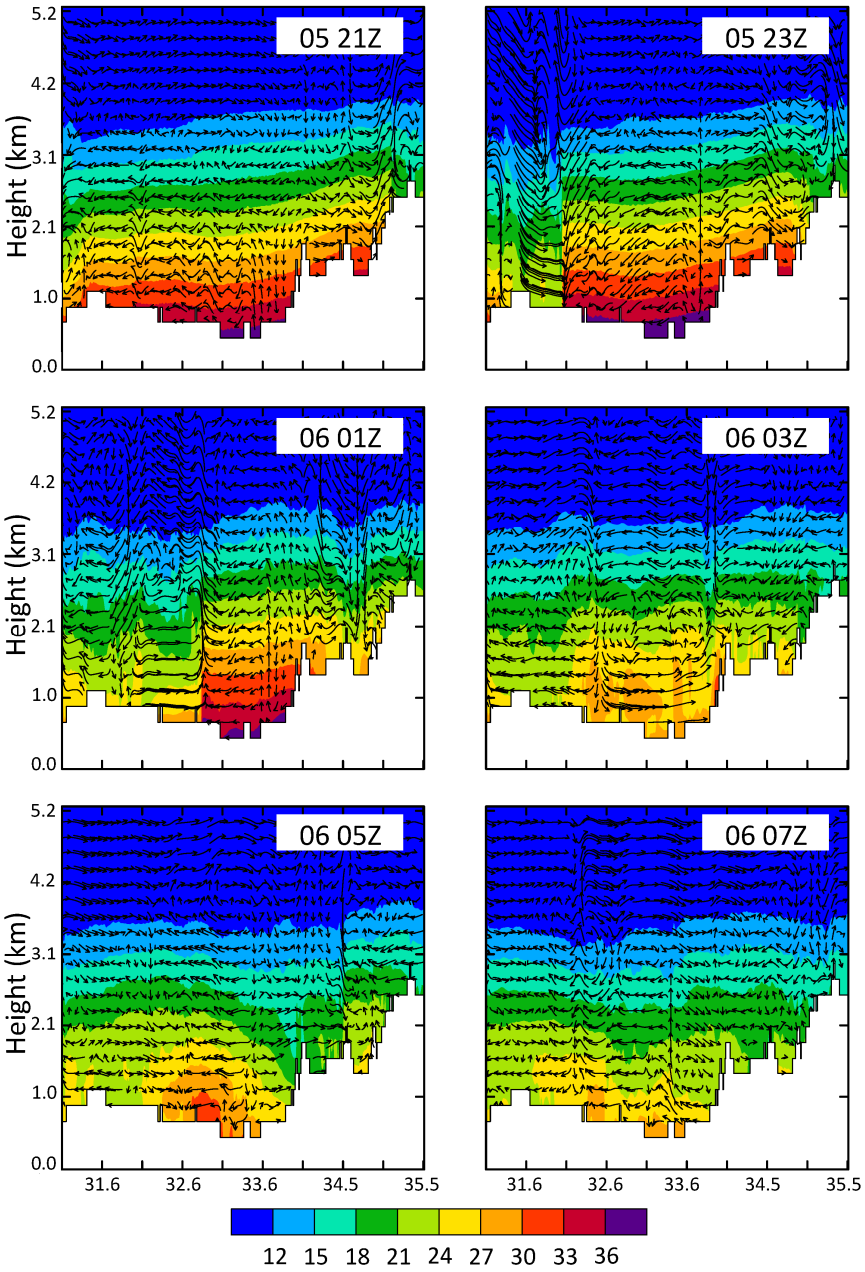

Figure 5. NU-WRF vertical cross section of temperature (°C) and the v-w component of wind vector (ms^{-1}) from 21 UTC July 5 to 07 UTC July 6, 2011. The cross section is along 112°W as shown in Figure 3a. The white area is the topography height.

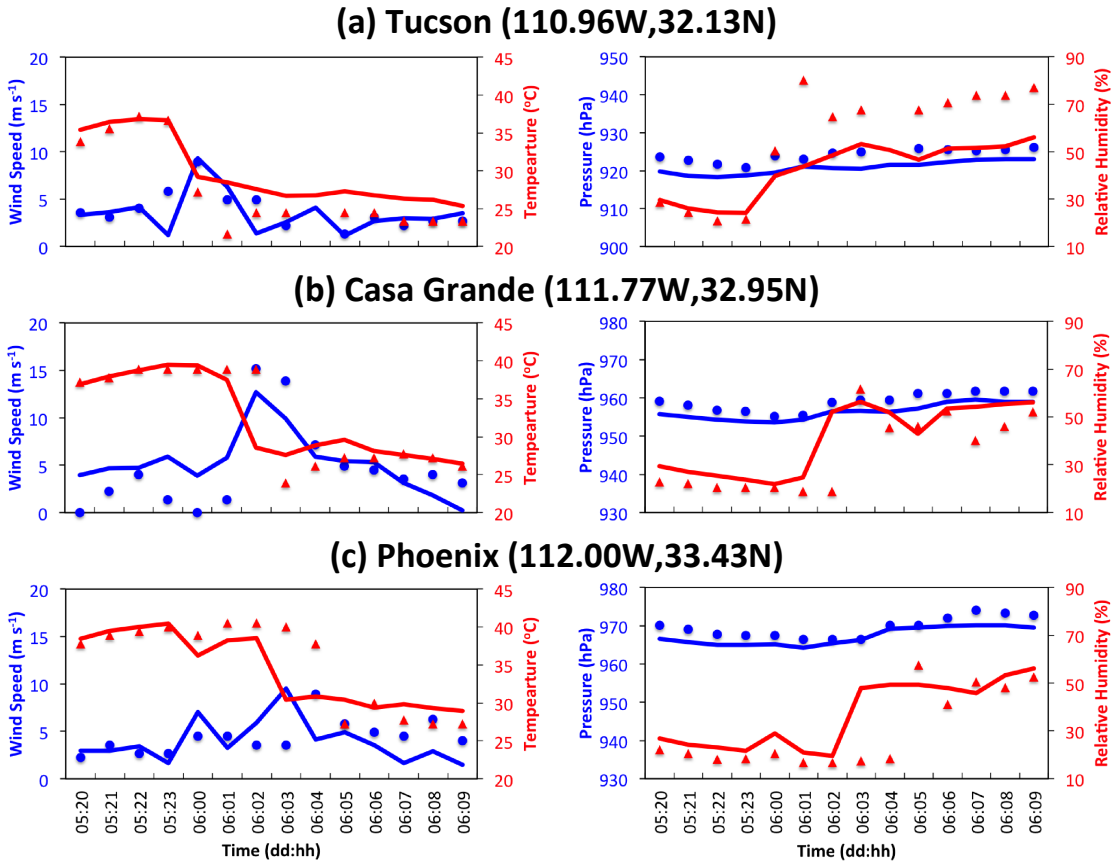

Figure 6. Meteorological variables from weather station measurements (dotted-line) and NU-WRF model (solid-line) from 20 UTC July 5 to 09 UTC July 6, 2011.

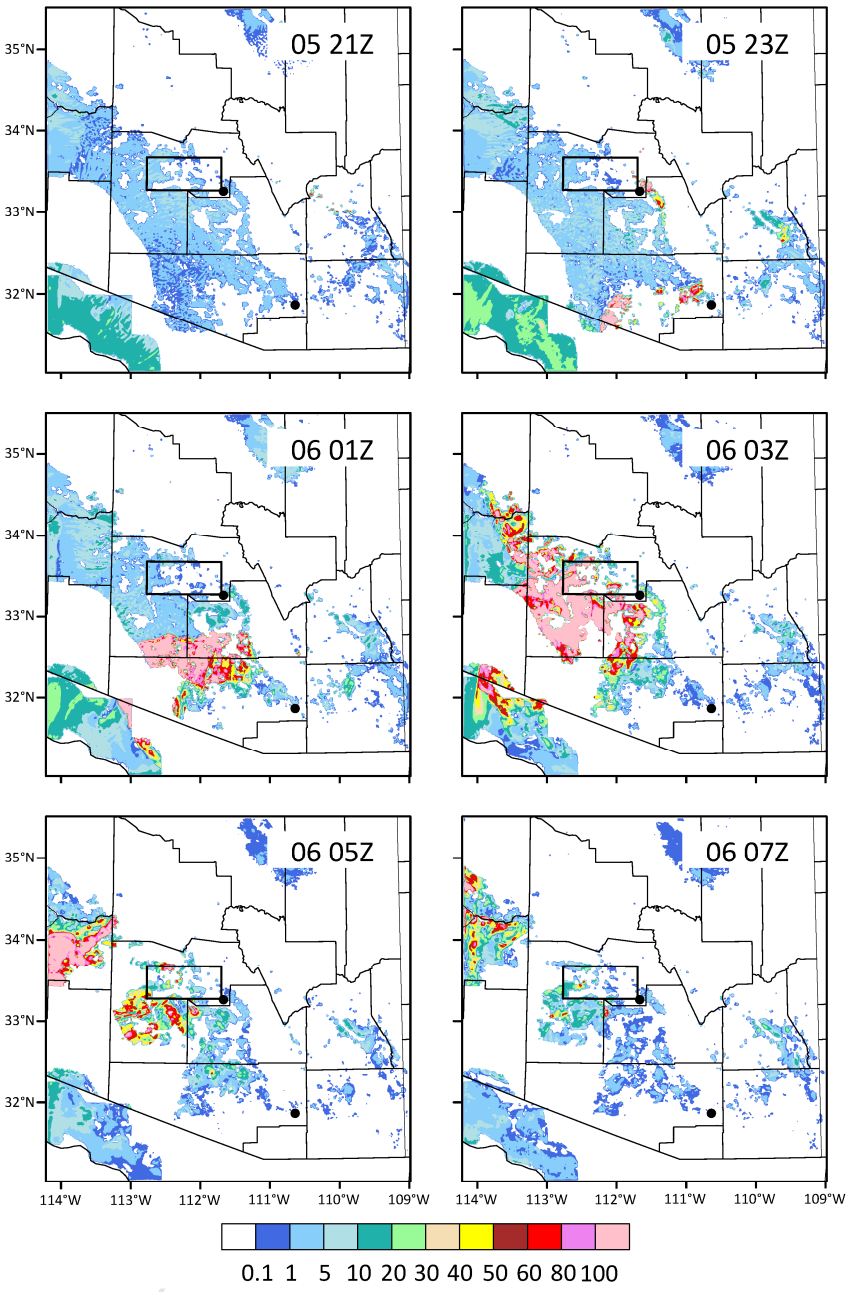

Figure 7. Same as Figure 4 except for dust emission (μg m^{-2} s^{-1}).

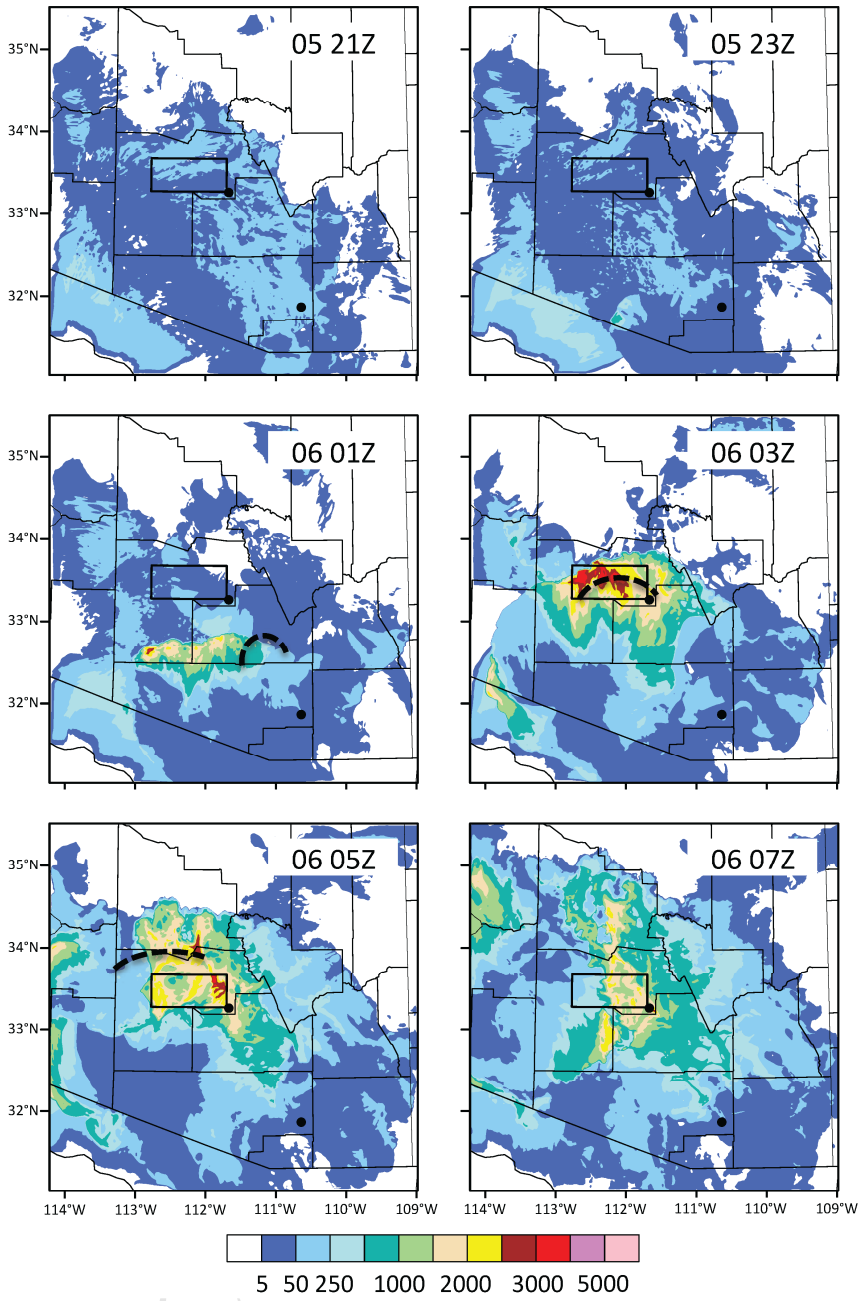

Figure 8. Same as Figure 4 except for surface dust PM10 concentration (μg m^{-3}).

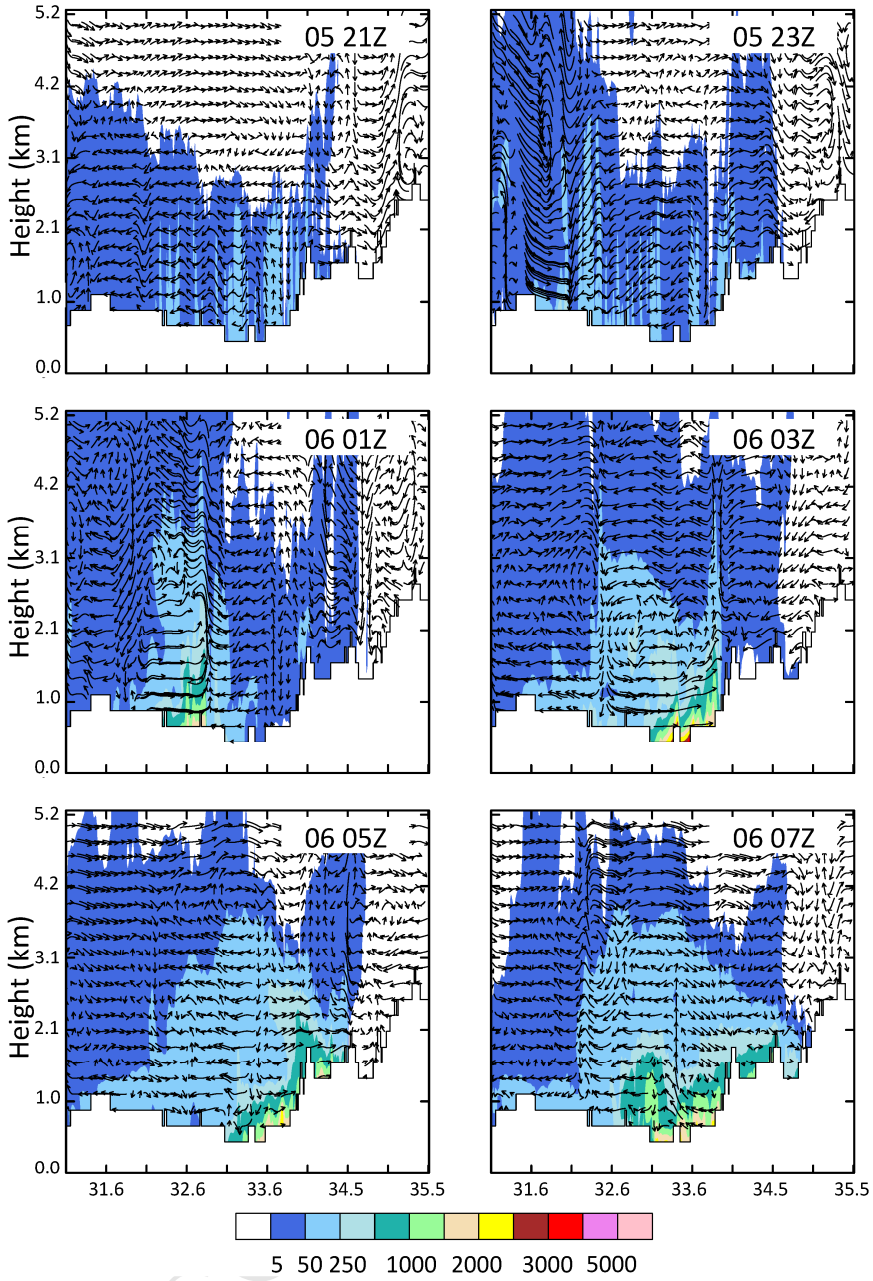

Figure 9. Same as Figure 5 except for surface dust PM10 concentration (μg m^{-3}).

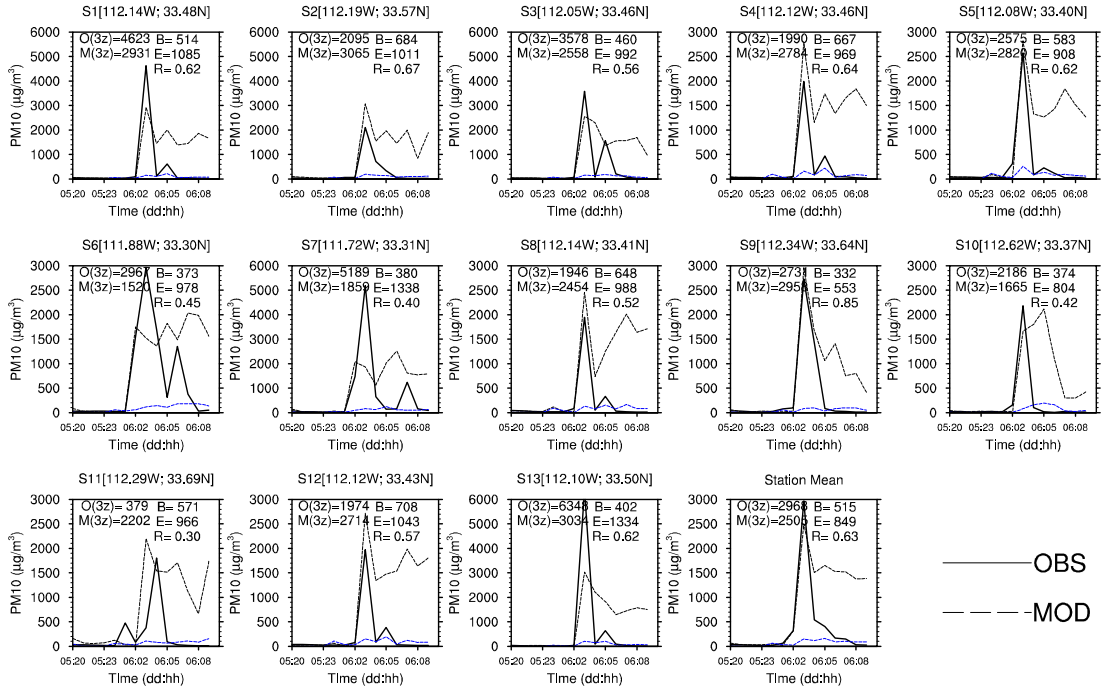

Figure 10. Time series of hourly mean observed PM10 and modeled dust PM10 at 13 EPA stations from 20 UTC July 5 to 09 UTC July 6, 2011. Static source results are shown in blue dashed lines. The panel on the bottom-right is the mean of 13 station values.

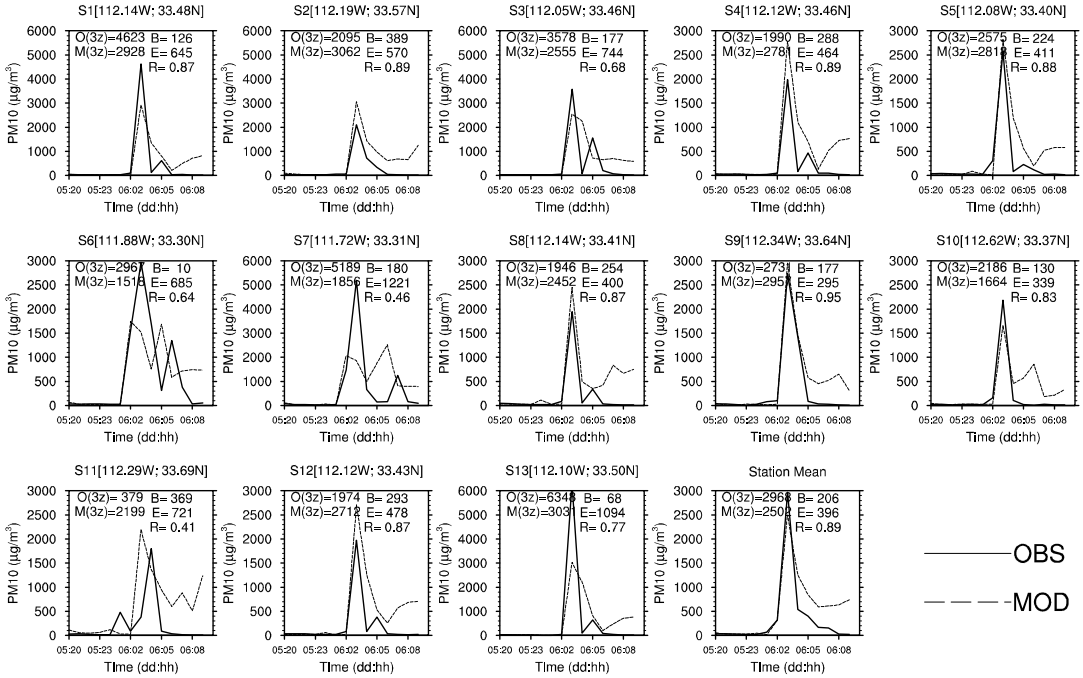

Figure 11. Time series of hourly mean observed PM10 and modeled dust PM10 at 13 EPA stations from 20 UTC July 5 to 09 UTC July 6, 2011. The panel on the bottom-right is the mean of 13 station values. In the model, emission is prohibited for 0300-0500 UTC July 6, 2011.

Highlights:

- A high-resolution dynamic dust source has been developed.
- New dust source better resolves the complex topographic distribution.
- A case study is successfully conducted with a strong dust storm in NU-WRF.